A Self-Synchronized Maximum-Power-Point Inductively Coupled Wireless Battery Charger for Embedded Microsensors

Nan Xing, *Graduate Student Member, IEEE*, and Gabriel A. Rincón-Mora, *Fellow, IEEE*

***Abstract*—Embedded microsensors are critical in today's fast-growing internet of things (IoT), as they provide an interface between the physical and digital worlds. An inductively coupled power receiver can replenish the onboard batteries and extend the microsensor's lifetime. Among all power receivers, the switched resonant half-bridge receiver outputs the highest power as it can operate beyond the circuit's breakdown adjust power transfer for maximum power point (MPP). However, switch synchronization and practical power transfer control remain two challenges. This paper presents a self-synchronization technique and a maximum-power-point adjustment control scheme for the switched resonant half-bridge wireless charger. The charger senses the high oscillation voltage without limiting the breakdown. Moreover, it can adjust the energy transfer frequency to reach and stay at the MPP when coupling varies. A prototype wireless charger is fabricated with 180 nm CMOS technology. The prototype charger, operating at 110 kHz, receives power up to 38 mm with a pair of 11.7 × 3.5 × 2.6 mm³ coils. Measurements show the charger outputs up to 89% of the available power across 0.067%–7.9% coupling range. The output power (in percentage of available power) and coupling range are 1.3× and 13× higher than the comparable state of the arts.**

***Index Terms*—Internet of things, embedded microsensors, inductively coupled, wireless charger, maximum output power.**

I. Powering Microsensors Inductively

Embedded microsensors are critical in the biomedical field and IoT [1-3]. However, these embedded microsensors' tiny onboard batteries often drain quickly. Harvesting ambient energy, such as light or motion, can help replenish the battery. However, such energy sources are not always available. Often, the only option left is to recharge the battery wirelessly using a pair of inductively coupled coils.

Fig. 1 illustrates a typical inductively powered microsystem. To transfer power, the transmitter coil L_T in Fig. 1 runs an AC current and generates a changing magnetic field in the nearby space. An adjacent receiver coil L_R captures the magnetic flux that L_T emits and couples an electromotive force (EMF) voltage v_E. From the coupled v_E, the wireless charger draws power to charge up the energy storage v_B, which supplies the microsystem's components, such as sensors, amplifiers, DSPs, etc. Designs in [3-6] combine the charging and supply stages into a single rectifying-regulating stage and remove the energy storage v_B. The single-stage rectifying-regulating stage is, in essence, a supply, as it provides the power that the load requires. However, most embedded microsensors are heavily duty-cycled to conserve energy [7]. Therefore, the microsensors' peak to average power ratio is often high [7]. Eliminating the intermediate energy storage v_B means the transmitter needs to instantaneously supply the peak power that the load requires, so the required peak transmitting power is high. However, the transmitting power for many biomedical implant applications is often very limited due to safety and health standards [8]. For such single-stage rectifying-regulating supply systems, the design goal is to maximize the power conversion efficiency (PCE). As the voltage and power are regulated at the output, maximizing the receiver's PCE minimizes the loss and conserves the most energy.

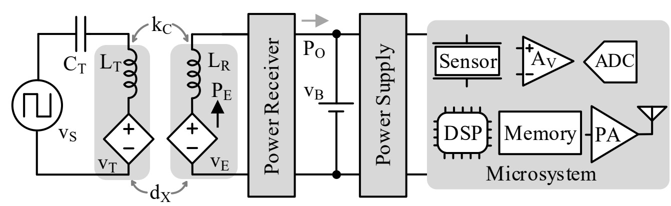

Fig. 1. Inductively powered microsystem.

The two-stage receiver and supply wireless power system in Fig. 1 works better for embedded microsensor applications. When the microsensor's load idles, the inductively coupled power receiver charges the intermediate energy storage v_B. When the load power peaks, like a cushion, the energy stored in v_B helps supply the load, so the transmitter does not need to instantaneously supply the full peak power. As a result, the required peak transmitting power is lower, which is more friendly for health and safety. The wireless power receiver in Fig. 1 is, in essence, a charger, as it extracts power from v_E to fill up the energy storage v_B. The design goal of the wireless charger is to maximize the output power to charge up the battery as fast as possible. Since the coupling between the coils is often very low in embedded microsensor applications [9], the power receiver barely loads the transmitter. So the transmitter power remains about the same. Maximizing the charger's output power equals maximizing the end-to-end efficiency.

The key to increasing the charger's drawn power is to apply a high alternating voltage across the receiving coil [10]. The high coil voltage boosts the current from the coil so the receiver can draw more power from v_E. For MPP, the applied voltage is raised to the breakdown or the conduction loss limit.

The resonant bridge/half-bridge charger uses LC resonance to boost L_R's voltage [11-14]. However, since the

The authors are with the School of Electrical and Computer Engineering at the Georgia Institute of Technology, Atlanta, GA 30332-0250 U.S.A. E-mail: nxing3@gatech.edu, Rincon-Mora@gatech.edu. Copyright © 2020 IEEE.

resonant capacitor and inductor are connected in parallel with the charger circuit. The maximum L_R voltage is limited by the charger circuit's breakdown. For standard deep-submicron CMOS circuits, this breakdown voltage is often low. The switched bridge [15-17] uses the rectified voltage to boost L_R's voltage. Similarly, the L_R's voltage is limited to the charger circuit's breakdown, as the rectified voltage connects with the circuit in parallel. The switched resonant half-bridge also uses LC resonance to boost L_R's voltage. However, the resonant capacitor C_R in Fig. 2, connected in series with the charger circuit, bears most of the L_R's voltage, so the breakdown limit is high. Therefore, the switched resonant half-bridge outputs the highest power without a buffer stage [10].

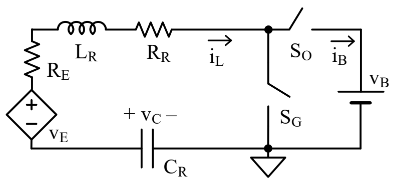

Fig. 2. Switched resonant half-bridge power stage.

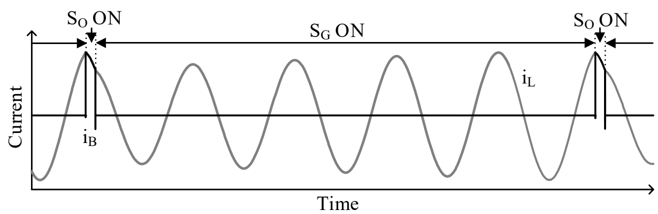

Fig. 3. Waveforms of the switched resonant half-bridge.

In a switched resonant half-bridge, the transmitter couples an open-circuit voltage v_E on the receiver coil L_R with a coupled resistance of R_E [18]. The coil L_R's effective series resistance (ESR) is R_R. L_R and C_R in Fig. 2 resonate at v_E's frequency. When the ground switch S_G is closed, v_E sources power into the LC tank. As S_G opens and the output switch S_O closes, the energy accumulated in the LC tank is partially drained to v_B. To raise i_L and boost power from v_E, the LC oscillation voltage v_C often exceeds the CMOS circuit's breakdown voltage V_{BD}, as S_G and S_O do not see the high voltage [10]. The over-V_{BD} flexibility extends the circuit's operational coupling range for maximum power point (MPP) [9]. For MPP, the S_G and S_O need to switch synchronously near i_L's peak, or, equivalently, v_C's zero, as shown in Fig. 3 [18]. The power stage proposed and analyzed in [9] and [18] outputs the highest MPP for a wide coupling range. However, challenges remain in the control implementation. First, synchronization is difficult as v_C can grow beyond v_{BD}. Second, the 3-variable MPP method in [18] needs to be simplified to reduce the area and power.

This paper addresses the control implementation challenges that [18] didn't address: it presents a self-synchronization technique and a simplified MPP adjustment scheme for the switched resonant half-bridge. The rest of the paper is organized as follows. Section II discusses the design and operation of the proposed self-synchronized switched resonant half-bridge charger that uses a high-voltage-sensing comparator for synchronization. The circuit implementation is described in Section III. Section IV assesses and compares the measured performance of the fabricated prototype. Conclusions are drawn in Section V.

II. Self-Synchronized Switched Resonant Half-Bridge

A. Synchronization

For MPP, the controller needs to synchronize the energy transfer with i_L's peak [18]. Sensing i_L directly is difficult and adding sensing resistance significantly lowers the available power from the receiver coil. The other option is to sense v_C, as i_L peaks when v_C crosses zero.

However, sensing v_C is also challenging, as v_C swings between positive and negative, and its magnitude can exceed the circuit's breakdown. The high voltage needs to be divided for the circuit to sense. Although the resistive divider in Fig. 4(a) can lower the voltage, its dividing ratio is fixed. As the coupling factor k_C varies for orders of magnitude in practical applications, the divided output v_{SEN} scales proportionally. As a result of the fixed dividing ratio, v_{SEN} is too high for breakdown at high k_C, but too low for the comparator to sense at low k_C.

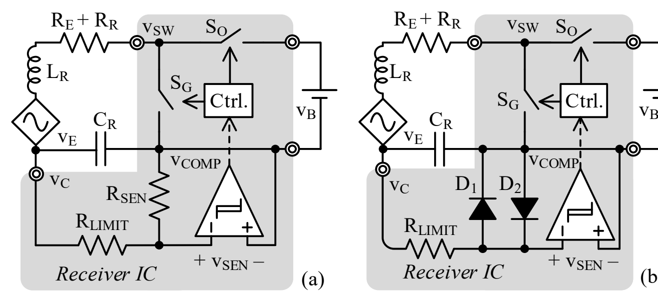

Fig. 4. Sensing high v_C with (a) resistive divider, and (b) a variable divider.

To reduce the coupling sensitivity, the diode-clamped voltage divider in Fig. 4(b) divides the voltage with a variable ratio. The circuit is composed of a pair of diodes D_1 and D_2 and a current limiting resistor R_{LIMIT}. When v_C's amplitude is within a diode voltage v_D, neither D_1 nor D_2 conducts, so v_{SEN} follows v_C. As v_C's amplitude grows beyond v_D, either D_1 or D_2 conducts current and clamps v_{SEN} at $\pm v_D$, as Fig.4(b) shows. In measurement, the coupling k_C grows from 0.067% to 7.9%, so v_C varies 36× from 0.56 V to 20 V. However, as Fig. 5 shows, the divided voltage v_{SEN} varies less than 2.7× in simulation due to the D_1 and D_2's voltage suppression. This way, the dividing ratio is low (<<1) at high v_C, but high (=1) at low v_C.

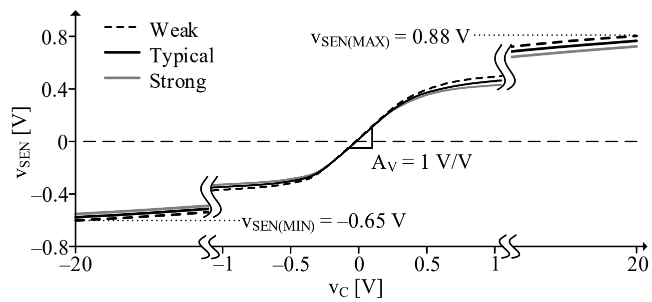

Fig. 5. Simulated output curve of the variable divider.

B. Maximum Power Point

The goal of the inductively coupled wireless charger design is to maximize its output power to charge up the battery as fast as possible. For MPP, the receiver needs to drain just enough energy such that the averaged $v_{C(PK)}$ over cycles is at its optimal level $v_{C(OPT)}$ [10], where

$$v_{C(OPT)} = \left(\frac{\pi L_R f_O}{R_E + R_R}\right) v_{E(PK)} . \quad (1)$$

To maintain the $v_{C(PK)}$ around $v_{C(OPT)}$, the energy transfer duration t_{ON} and energy transfer frequency f_X can be adjusted. Although adjusting both t_{ON} and f_X gives the highest power, it complicates the controller design. Fortunately, near MPP, P_O is not sensitive to t_{ON} variation. In [18], $P_{O(MPP)}$ is lowered by less than 1.3% even if t_{ON} is 24% off its optimal value. Adjusting f_X alone gives about the same $P_{O(MPP)}$ while simplifying control.

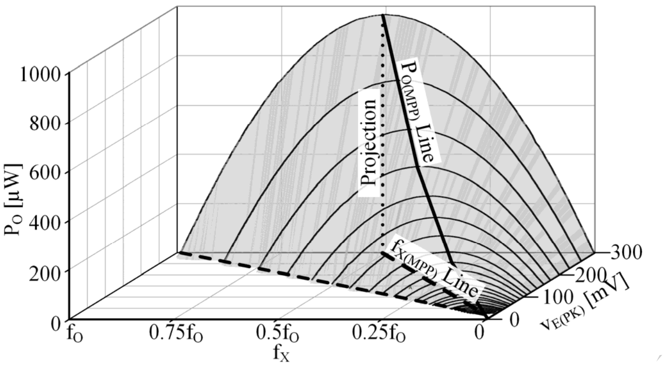

Fig. 6. Measured P_O across $v_{E(PK)}$ and f_X.

Fig. 6 shows how P_O varies across f_X at different $v_{E(PK)}$. At very low f_X, the battery draws little power from the LC, so the energy in the LC builds up high. As a result, the quadratically growing ohmic loss dominates so the output power is low. Similarly, at high f_X, the battery draws too much power from the LC, so little energy remains in the LC tank. As a result, v_C stays below $v_{C(OPT)}$. P_O maximizes at $f_{X(MPP)}$ when v_C averages $v_{C(OPT)}$. The MPP theory in [18] predicts that $f_{X(MPP)}$ grows proportionally with $v_{E(PK)}$:

$$f_{X(MPP)} = \left(\frac{\pi}{4}\right)\left(\frac{v_{E(PK)}}{v_B}\right) \Big/ \sin\left[\left(\frac{t_{ON}}{t_O}\right)\pi\right] \propto v_{E(PK)} . \quad (2)$$

C. Full System

The switched resonant half-bridge in Fig. 7 uses a resonant tank L_R–C_R to boost current and power from v_E. The L_R and C_R are tuned to v_E's frequency f_O, so v_E constantly sources power into the LC tank. R_E represents the coupled resistance from the transmitter, while R_R is the ESR of L_R at f_O.

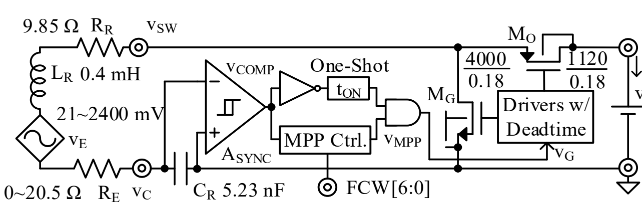

Fig. 7. Switched resonant half-bridge wireless charger.

To transfer energy, the power stage alternately switches between two modes: receiving energy from v_E and transferring received energy to v_B. The ground switch M_G closes for most of the cycle t_X, so L_R–C_R receives and stores energy from v_E. Then, M_G is turned off and the output switch M_O is turned on for t_{ON}, so the energy accumulated is transferred to the battery v_B. The deadtime logic inserts around 1 ns delay so M_G or M_O only turns on when the other switch is completely off. This prevents both switches from turning on at the same time and discharge the battery. The ground switch M_G and the output switch M_O are 4000 µm and 1120 µm wide, respectively. The sizes are optimized to minimize the losses for 300 µW, which is the most probable power level for targeted glucose and blood-pressure sensing applications [2, 19].

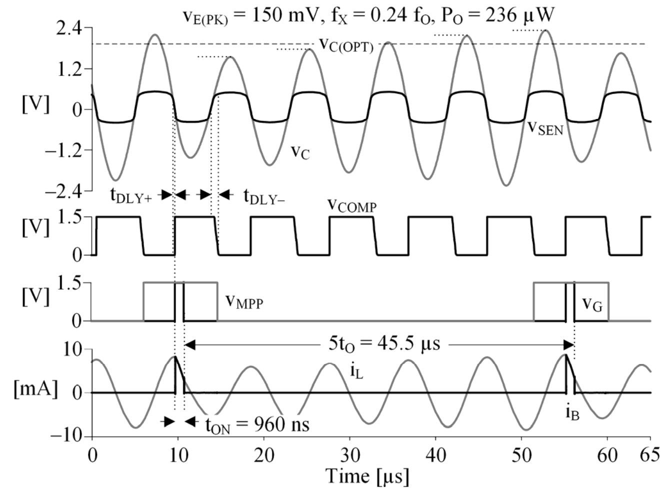

Fig. 8. Simulated wireless charger waveforms at 150 mV $v_{E(PK)}$.

For MPP, the energy transfer needs to be synchronized with the oscillation. For this, the synchronizing comparator A_{SYNC} in Fig. 7 detects the zero crossings of v_C in the negative direction. To transfer power near i_L's peak, the comparator is designed to optimize its rising edge delay t_{DLY}^{+} over its edge delay t_{DLY}^{-}, so $t_{DLY}^{+} << t_{DLY}^{-}$. Once a crossing is detected, a one-shot circuit triggers a fixed pulse t_{ON}, as Fig. 8 shows. The charger only transfers power to the battery when the gating signal v_{MPP} is high. The MPP controller uses a 7-bit frequency control word FCW[6:0] to adjust the average number of cycles between energy transfers and in a delta-sigma fashion. The detailed operation will be discussed in the next section.

III. Circuit Implementation

A. Synchronizing Comparator

To protect the sensing circuit from breakdown, a voltage divider owers v_C to v_{SEN}, as shown in Fig. 9. Diode-connected NMOS M_{D1} and M_{D2} in Fig. 9 replace the diodes D_1 and D_2 in Fig. 4(b). The comparator in Fig. 9 compares v_{SEN} with the ground to detect v_C's zero crossings and synchronizes the energy transfer. The comparator needs to (i) take negative input as v_{DIV} swings from $-v_D$ to $+v_D$, and (ii) minimize the v_C's falling edge delay t_{DLY-} for MPP. For (i), a PMOS pair, M_1 and M_2, is used. M_1's gate is grounded which generates a bias voltage v_B for M_4's pull-up path. Above-zero v_{DIV} crushes M_4's v_{GS}, so M_6 pulls v_{O1} up slowly with fixed 180 nA. As v_{DIV} drops below zero, M_2's current grows quadratically with the voltage drop and pulls v_{O1} down quickly. As v_{DIV} drops below zero, M_2's source and body follow, preventing the circuit from breakdown. For (ii), a secondary common-source stage M_{10} expedites v_{COMP}'s pulling-up as v_{COMP1} falls. Combining that v_{COMP1} pulls down fast and v_{COMP} pulls up fast, the measured t_{DLY-} (120 ns ~ 180 ns) is much shorter than t_{DLY+} (1 µs ~ 1.8 µs), as Fig. 8 shows.

The voltage divider induces loss as the R_{LIMIT} steals and burns a fraction of i_L. At high v_C, ignoring the voltage drop on the diodes, the fractional loss that parallel R_{LIMIT} induces is equivalent to a series resistance of 0.3Ω [20], which lowers $P_{O(MPP)}$ by 3%. At low v_C, as the diodes' voltage drop lowers the current across R_{LIMIT} more, R_{LIMIT}'s loss is less than 3%. A larger R_{LIMIT} lowers the current stolen and the loss. However, larger R_{LIMIT} also adds more parasitic capacitance at v_{SEN}, causing more delay. An offset time that equals 3% of the period lowers the output power by 4% [18]. A 250 kΩ R_{LIMIT} is chosen to keep the RC delay within 3% of the oscillation period.

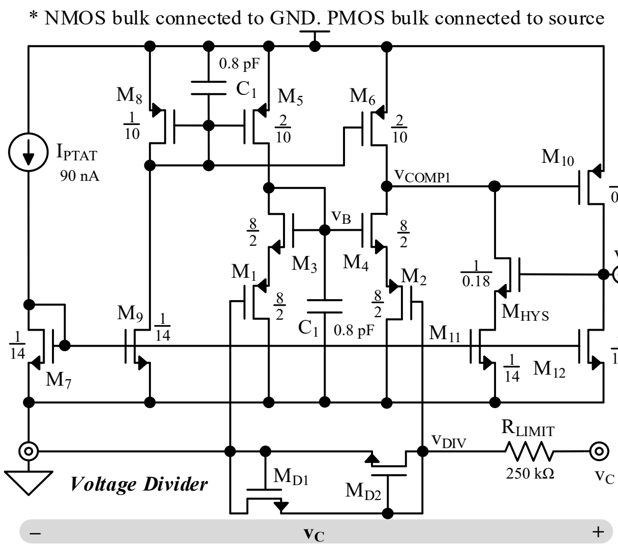

Fig. 9. Synchronizer circuit with the variable divider

B. MPP Controller

The MPP controller is implemented with a 7-bit-input, 1-bit-output digital-to-digital delta-sigma modulator frequently found in fractional-N PLL designs [21]-[22], as shown in Fig. 10. Each time the synchronizing comparator's output v_{COMP} toggles in the negative direction, the full adder self-adds the 7-bit frequency control word FCW to the 8-bit register array ACC. This way, ACC accumulates FCW each cycle, as Fig. 11 shows. Once ACC's most significant bit (MSB), v_{MPP}, toggles high, it enables the energy transfer in the next coming cycle. The 7 least significant bits (LSBs) are fed back to the full adder's input for the next cycle's accumulation in a delta-sigma fashion. Since v_{ACC} self-accumulates v_{FX} each time and its MSB toggles once the accumulation reaches 128, the averaged energy transfer frequency is

$$f_{X(MPP)} = \frac{v_{FX}}{128} f_O \,. \tag{3}$$

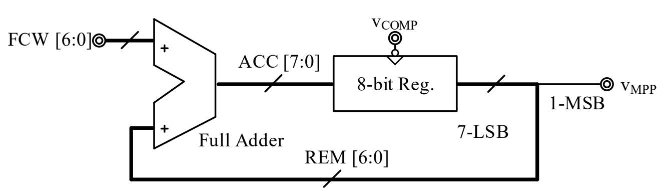

Fig. 10. Delta-sigma MPP controller.

This way, f_X can be adjusted with 1/128 f_O resolution. Compared to skipping an integer number of cycles [23], the delta-sigma modulator allows skipping a fractional number of cycles. Details including waveforms of skipping a fractional number of cycles will be discussed in the next section.

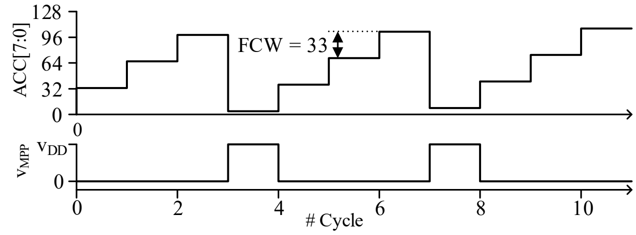

Fig. 11. Waveforms of the MPP controller.

IV. Measurements

A. Prototype

To demonstrate the charger's functionality and performance, a prototype is built with 180-nm CMOS technology. The charger IC, as shown in Fig. 12, integrates the power stage (M_G, M_O, and the driver) and the synchronizer (I_{PTAT}, A_{SYNC}, V_{DIV}) while occupying only 220 μm × 381 μm of silicon area. The prototype operates at 110 kHz, which is much lower compared to the 6.78 MHz used in the previous design [9]. The lower frequency operation greatly reduces the power consumption of the synchronizing comparator. The downside is that the resonant capacitor C_R increases to 5.23 nF so it cannot be integrated on-chip. However, the off-chip C_R measures only 1.6 × 0.8 × 1.6 mm^3, which adds a limited volume to the overall system. The wireless charger uses the 0.4 mH Coilcraft 4513TC as the receiver coil that measures 11.7 × 3.5 × 2.6 mm^3. This is smaller than the 4.7 μH Coilcraft PA6512-AE used in [9]. The MPP control and one-shot circuit in Fig. 2 are implemented on an FPGA for testing flexibility. The MPP control is fully synthesizable and can be migrated on-chip easily.

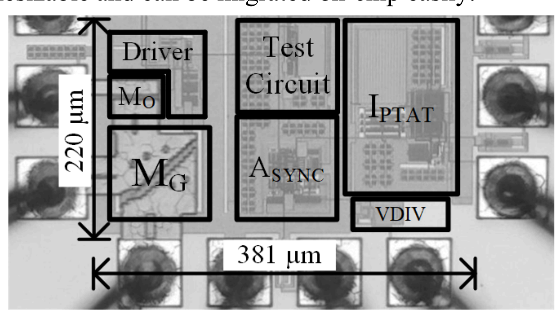

Fig. 12. Photos of the wireless charger IC.

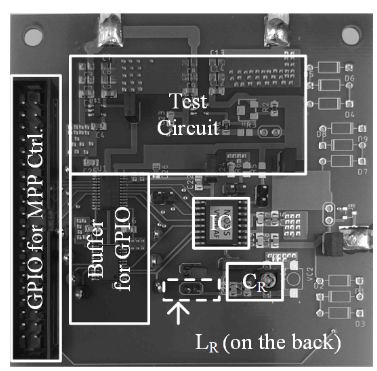

Fig. 13. Photos of the wireless charger PCB.

Fig. 13 shows the photo of the charger prototype PCB. The FPGA and the charger PCB are connected via the GPIO port, as shown in Fig. 13. The linear stage in Fig.14 adjusts the distance between the wireless charger and the source from 0 to 38 mm. As a result, the coupled open-circuit voltage v_E on the receiver coil ranges from 24 mV to 2.8 V. The transmitter couples up to 20.5 Ω back on the receiver coil.

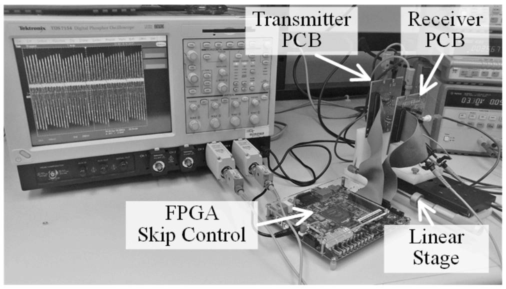

(a) Measurement setup

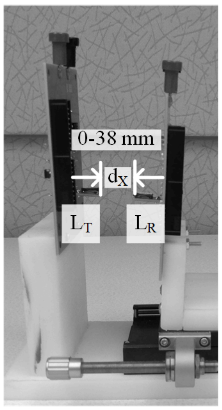

(a) Linear stage that adjusts d_X from 0 to 38 mm

Fig. 14. The measurement setup and the linear stage.

Resonance boosts power but puts electrical stress on the receiver. The electrical stress grows with the oscillation until saturated by the ohmic loss [10]. When saturated, the oscillation voltage is twice as high as $v_{C(OPT)}$ [10], so

$$v_{C(MAX)} = 2v_{C(OPT)} = \left(\frac{sL_R}{R_R + R_E}\right) v_{E(PK)} , \tag{4}$$

where sL_R is L_R's impedance at f_O. As C_R and L_R resonate at f_O, $v_C + v_L \approx 0$. Therefore,

$$i_{L(MAX)} = \frac{v_{E(PK)}}{R_E + R_R} . \tag{5}$$

With the measured $v_{E(PK)}$ and R_E, C_R and L_R's voltage and current stress can be calculated using (4) and (5). In measurement, $v_{C(MAX)}$ ranges 20~0.57 V, and $i_{L(MAX)}$ ranges 74~2.1 mA across 0~38 mm.

On the transmitter side, a power inverter (modeled as v_S in Fig. 1) drives the L_TC_T resonant tank. As the receiver draws little power the current and voltage stress on L_T and C_T relatively constant across d_X. Transmitter's $i_{T(MAX)}$ and $v_{T(MAX)}$ can be calculated similarly as the receiver:

$$i_{T(MAX)} = \left(\frac{4}{\pi}\right)\left(\frac{v_{S(PK)}}{R_S + R_T}\right) , \tag{6}$$

$$v_{T(MAX)} = \left(\frac{sL_T}{R_S + R_T}\right)\left(\frac{4}{\pi}\right) v_{S(PK)} , \tag{7}$$

where R_T is the source impedance of the driving inverter. Compared to (4) and (5), a $4/\pi$ term is multiplied to $v_{S(PK)}$ as the sinusoidal fundamental tone of the square-wave v_S is $4/\pi$ times higher [18]. In the measurement setup, $v_{S(PK)} = 3.3$V, $R_S = 5.6$ Ω, and $R_T = 10.2$ Ω. The derived $v_{T(MAX)}$ and $i_{T(MAX)}$ are 73 V and 265 mA, respectively.

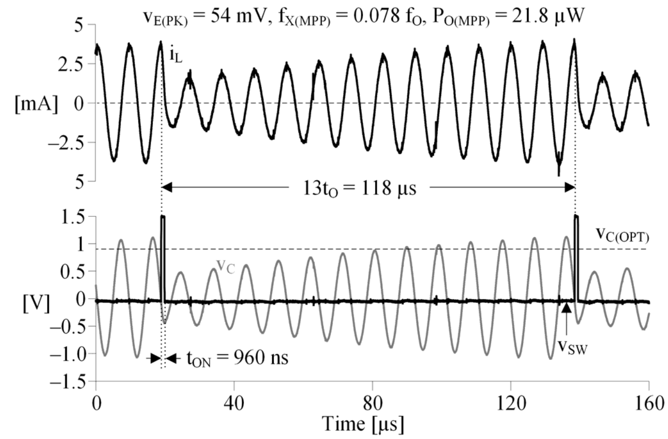

Fig. 15. Measured MPP receiver waveforms when k_C = 0.15%.

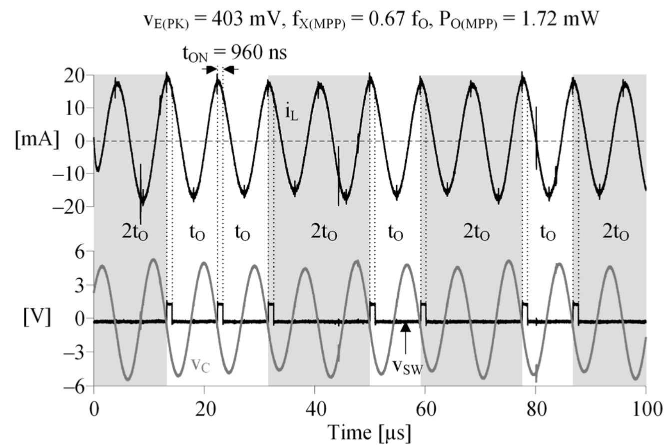

Fig. 16. Measured MPP receiver waveforms when k_C = 1.1%.

Fig. 15 and Fig. 16 show the measured v_{SW}, v_C, and i_L waveforms at MPP when the receiver is 28 mm and 10 mm away from the power source. The couplings are 0.15% and 1.1%, respectively. When the coupling is weak, the charger transfer energy less frequently to allow energy to build up in the LC tank and raise L_R's voltage. At 0.15%, the wireless charger on average skips 12.8 cycles between energy transfer for MPP. In other words, $f_{X(MPP)} = 0.078\ f_O$. When the coupling is high, the charger transfer energy more frequently to avoid LC energy build up too high and causes excessive conduction loss on L_R. At 1.1% coupling, the wireless charger transfers energy every one or two cycles, such that the average number of cycles between energy transfer is 1.5. So the effective MPP transfer frequency $f_{X(MPP)} = 0.67\ f_O$.

B. *Charging Profile*

To evaluate the charger's performance, a charging test is performed that charges up a 1.1 µF capacitor C_O from 1 V to 1.8 V when the receiver is 13 mm, 18 mm, 23 mm, and 28 mm away from the power source. At the above distances, the receiver fully charges C_O in 3.6 ms, 7.9 ms, 20 ms, and 63 ms, respectively. The corresponding charging currents are 500 µA, 250 µA, 9.9 µA, 3.2 µA, respectively, as shown in Fig. 17.

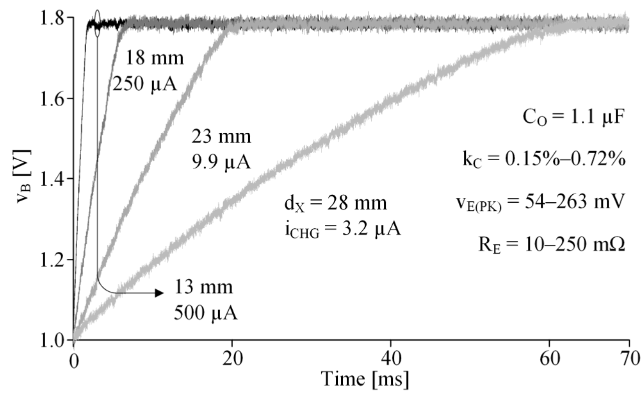

Fig. 17. Measured charging waveforms at 13~28 mm distance.

C. Ideality Factor

The maximum output power $P_{O(MPP)}$ is the key performance of the wireless charger. However, different wireless chargers' $P_{O(MPP)}$ is not comparable, as $P_{O(MPP)}$ scales with the transmitter's power and coupling. To assess the relative performance of the wireless charger, $P_{O(MPP)}$ needs to be normalized. Maximum available power $P_{O(MAX)}$ defines the highest power the receiver can possibly draw from the transmitter at the given coupling:

$$P_{O(MAX)} = \left(\frac{0.5v_{E(PK)}}{\sqrt{2}}\right)^2 \left(\frac{1}{R_R + R_E}\right), \quad (8)$$

$P_{O(MAX)}$ typically drops with $d_X{}^6$ when distantly coupled [24]. The ideality factor η_I references $P_{O(MPP)}$ to $P_{O(MAX)}$ and normalizes $P_{O(MPP)}$ with non-receiver variables:

$$\eta_I = \frac{P_{O(MPP)}}{P_{O(MAX)}}. \quad (9)$$

Fig. 18 shows the measured η_I when d_X ranges from 0–38 mm. Ideality η_I is high (> 60%) at 7 – 27 mm. Past 27 mm, η_I gradually drops to zero. This is because, as the power source separates further from the wireless charger, it couples less v_E on the receiving coil and, according to (2), the wireless charger skips more cycles between energy transfer for MPP. Although on average, v_C is at $v_{C(OPT)}$, each cycle's $v_{C(PK)}$ deviates further from $v_{C(OPT)}$, the non-linear loss [18] caused by the deviation grows and lowers η_I.

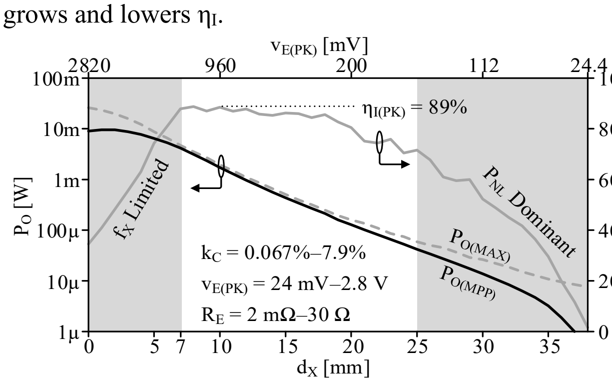

Fig. 18. Measured ideality factor across power transmission distance d_X.

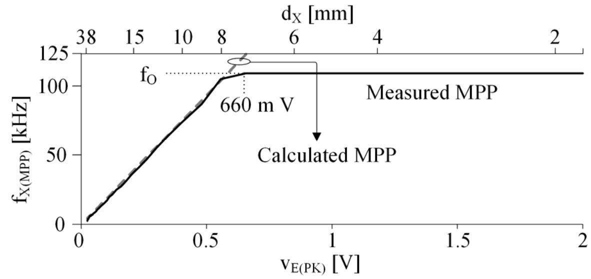

Fig. 19. Measured $f_{X(MPP)}$ across $v_{E(PK)}$.

On the other end, when d_X is shorter than 7 mm, η_I is also low. This is because, as the transmitting source couples more v_E on the receiving coil, $f_{X(MPP)}$ scales up linearly and eventually reaches its maximum limit: f_O. Beyond that, the MPP controller can no longer adjust f_X to the desired $f_{X(MPP)}$, so η_I starts to drop. As shown in Fig. 19, $f_{X(MPP)}$ reaches f_O as $v_{E(PK)}$ grows above 0.58 V. Then $f_{X(MPP)}$ is capped to f_O, and $P_{O(MPP)}$ becomes f_X-limited. Transferring energy for a longer duration t_{ON} improves η_I when the coupling is high and $P_{O(MPP)}$ is f_X-limited. However, for targeted biomedical implant applications, high coupling is unlikely. Plus, adjustable t_{ON} requires additional circuitry and quiescent power. So t_{ON} is fixed at 960 ns, which is the optimal t_{ON} when coupling k_C is halfway (in log scale) across the 0.067%-7.9% range.

Fig. 20 shows the loss breakdown of the proposed inductively coupled wireless charger. Among all the losses, the nonlinear loss P_{NL} dominates when k_C is lower than 0.3% or higher than 2%. At low k_C, the power receiver skips more cycles for MPP [18], so P_{NL} is high. At high k_C, $P_{O(MPP)}$ becomes f_X-limited, so P_{NL} is also high. The high-voltage-sensing circuit consumes $P_{R(SEN)}$, as R_{LIMIT} steers away a fraction of the LC tank's current. However, when v_C drops below a diode voltage, the diodes D_1 and D_2 conduct little current, so $P_{R(SEN)}$ gradually drops to zero at low k_C. The quiescent loss P_Q and charge loss P_C do not scale proportionally with k_C. Therefore, their portion grows at low k_C.

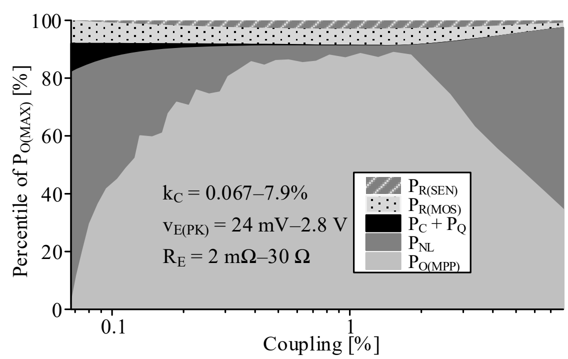

Fig. 20. Measured $f_{X(MPP)}$ across $v_{E(PK)}$.

The power and ideality in Fig. 19 are measured when the transmitter coil L_T and the receiver coil L_R align in the center. In real applications, the coils' centers often misalign by a lateral distance d_Y. The math model in [25] predicts the magnetic field H_Z that L_R captures at distance d_X with lateral misalignment d_Y:

$$H_Z = \left(\frac{I_T}{2\pi d_Y}\right)\sqrt{\frac{m}{4r_T d_Y}}\left[d_Y K + \frac{r_T m - (2-m)d_Y}{2-2m}E\right], \quad (10)$$

TABLE I: RELATIVE PERFORMANCE

	JSSC '13 [16]	TCAS II '13 [17]	JESTPE '13 [18]	AICASP '20 [3]	TCAS I '16 [30]	TCAS II '18 [9]	JSSC '16 [31]	This Work
Receiver Type	Switched Bridge				Switched Resonant Half-Bridge			
Tech. (μm)	0.18	0.18	0.18	0.5	Board	0.18	0.18	0.18
Silicon Area (mm^2)	0.49	0.245	0.26	2.25	–	0.471	0.544	0.084
Tx Coil Size	224 mm^3	224 mm^3	–	100 mm^3	28900 mm^2	633 mm^3	–	106 mm^3
Rx Coil Size	106 mm^3	106 mm^3	106 mm^3	25 mm^3	900 mm^2	633 mm^3	106 mm^3	106 mm^3
d_X (mm)	0–11	0–11	10–50	0–8	70	13–38	85	0–38
f_O (MHz)	0.125	0.125	0.125	13.56	1	6.78	0.05	0.11
k_C (%)	0.59–6.7	0.9–7.6	0.15–1.35	–	1.3	0.09–1.1	–	0.067–7.9
k_C Attenuation w/ d_Y (dB)	–	–	–	–	–	–	–	–20 @ $d_X = d_Y$
$v_{E(PK)}$ (mV)	39.5–386	46–480	66–585	–	41	18.5–282	–	24–2880
$P_{O(MPP)}$ (μW)	0–224	26.6–830	16–557	5830	96.1	1.2–1340	0–2.84	0.1–26000
Over-V_{BD} Operation	No	No	No	No	No	Yes	No	Yes
Self-Synchronized	No	No	Yes	Yes	No	No	Yes	Yes
Closed-Loop MPPT	No	No	No	Yes	No	No	Yes	No
$\eta_{I(PK)}$ (%)	30.9*	46.9*	28.6*	–	42.9	84.8	67.7	88.8
k_C Range	9.8×	8.4×	9×	–	–	12.2×	7.1×	118×

*Ideality inferred from the reported $P_{O(MPP)}$, $v_{E(PK)}$, R_R, and estimated R_E, using (3) and (4). R_E is estimated as in [12].

$$m = \frac{4r_T d_Y}{(r_T + d_Y)^2 + d_X^2} \quad . \tag{11}$$

Here, r_T is the radius of the transmitter coil. K and E are the complete elliptic integrals of the first and second kind [25]. Lateral misalignment attenuates H_Z and thus lowers the coupling k_C. Fig. 21 shows how k_C attenuates with d_Y at 10, 20, and 30-mm separation using Eqn. (10)'s prediction. At $d_Y = d_X$, $v_{E(PK)}$ attenuates ~20dB across different d_X. Ideality $\eta_{I(PK)}$ for misaligned coils can be estimated using Fig. 20 and Fig. 21. First, use Fig. 21 to estimate the attenuated k_C at d_Y. Then, map the attenuated k_C onto Fig. 20 to find the estimated $\eta_{I(PK)}$.

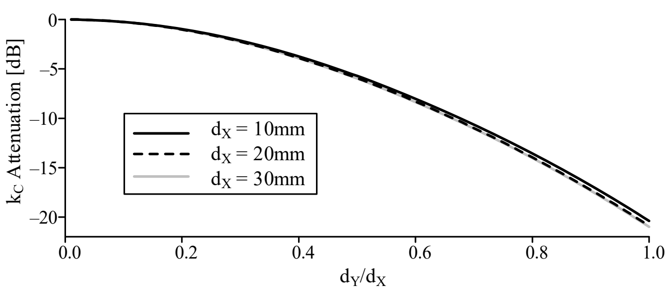

Fig. 21. Measured $f_{X(MPP)}$ across $v_{E(PK)}$.

D. Relative Performance

Fig. 22 compares the proposed charger's η_I across k_C with the state of the art. For a fair comparison, single-stage wireless rectifying-regulating supply systems [14, 26-29] are excluded, as their design goal is to maximize the PCE of the receiver instead of MPP. The wireless chargers in [30], [9], and [31] are based on switched resonant half-bridge and its variations. Although [9] achieves an ideality as high as 85%, the charger cannot self-synchronize. Therefore, the system is incomplete. The charger in [30] has no synchronizer either. Plus, as the charger completely drains the LC tank's energy each time, the energy transfer is not optimal. So ideality is low at 42.9%. The charger in [31] is self-synchronized and achieves 67.7% of η_I. However, its power stage cannot operate beyond the circuit's breakdown, so the coupling range is 16× narrower. The charger in [31] includes a maximum power point tracking (MPPT) that this design does not have. However, the MPPT is based on a one-time calibration, so it does not affect the ideality. [31] is not included in Fig. 22, as the coupling information cannot be extracted from the paper.

The switched bridges in [15], [16], and [17] energizes and de-energizes L_R directly with the battery. As the switches in the switched bridge see the inductor voltage, the circuit cannot operate beyond breakdown. So the workable coupling ranges are much lower compared to the proposed design. The chargers in [15] and [16] cannot self-synchronize, so the systems are incomplete. Although the charger in [17] includes an integrated synchronizer, the synchronizer needs to break the charging operation, resulting in additional opportunity loss. As a result, its $\eta_{I(PK)}$ is the lowest at 28.6%.

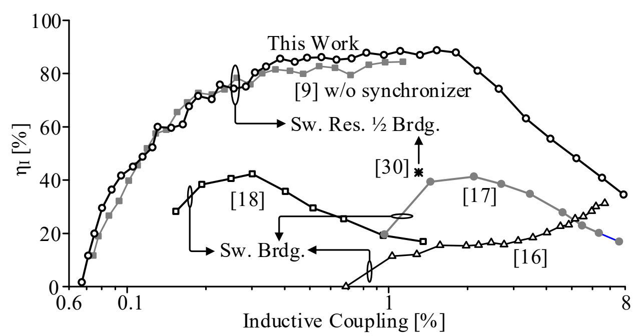

Fig. 22. Measured η_I compared with the state of the arts.

Table I summarizes and compares the performance of the proposed design with the state of the arts. Although the design in [3] is a supply, it adjusts the transmitter power to deliver the right amount of power to the load. In other words, it achieves MPP the same way as a charger and is thus comparable. The chargers in [30], [9], [15], and [16] are incomplete as they do not include a synchronizer. Still, among all designs, the proposed design achieves the highest η_I of 89% and the widest k_C range of 118×. Compared to other self-synchronized wireless chargers, the proposed wireless charger improves η_I and k_C range by 1.3× and 13×, respectively.

V. Conclusions

Embedded microsensors are critical blocks in the biomedical field as well as in the IoT. Inductively coupled battery charger greatly extends the microsensors' lifetime. For practical applications, the charger needs to output the highest power possible over a wide coupling range. This paper proposes a self-synchronized switched resonant half-bridge inductively coupled battery charger. The charger's power stage's series resonant capacitor withstands the high coil voltage needed to boost output power. The proposed charger also adjusts energy transfer patterns so the output power can stay at MPP as coupling varies orders of magnitude. Finally, the charger addresses the challenge of synchronization, as the voltage being sensed for synchronization can far exceed the CMOS circuit's breakdown. A prototype charger is fabricated using 180-nm CMOS technology. Measurements show that the proposed charger improves the output power and workable coupling range by 1.3× and 13× over the state of the art.

Acknowledgment

The authors thank Texas Instruments (TI) for sponsoring this research and Dr. Orlando Lazaro, Dr. Andres Blanco, and Dr. Jeff Morroni for their support and advice.

References

[1] M. Kang, E. Park, *et al.*, "Recent patient health monitoring Platforms incorporating internet of things-enabled smart devices," *International Neurourology Journal,* vol. 22, no. 2, pp. 76-82, 2018.

[2] M.M. Ahmadi, and G.A. Jullien, "A wireless-implantable microsystem for continuous blood glucose monitoring," *IEEE Transactions on Biomedical Circuits and Systems,* vol. 3, no. 3, pp. 169-180, 2009.

[3] N.T. Tasneem, D.K. Biswas, *et al.*, "A CMOS closed-loop miniaturized wireless power transfer system for brain implant applications," *Analog Integrated Circuits and Signal Processing,* October 2020.

[4] H.S. Gougheri, and M. Kiani, "An inductive voltage-/current-mode integrated power management with seamless mode transition and energy recycling," *IEEE Journal of Solid-State Circuits,* vol. 54, no. 3, pp. 874-884, 2019.

[5] Q.W. Low, and L. Siek, "A single-stage dual-output tri-mode AC-DC regulator for inductively powered application," *IEEE Transactions on Circuits and Systems I: Regular Papers,* vol. 66, no. 9, pp. 3620-3630, 2019.

[6] H.S. Gougheri, P. Graybill, *et al.*, "A dual-output reconfigurable shared-inductor boost-converter/current-code inductive power management ASIC with 750% extended output-power range, adaptive switching control, and voltage-power regulation," *IEEE Transactions on Biomedical Circuits and Systems,* vol. 13, no. 5, pp. 1075-1086, 2019.

[7] Y. Zhang, F. Zhang, *et al.*, "A batteryless 19 w MICS/ISM-band energy harvesting body sensor node SoC for ExG applications," *IEEE Journal of Solid-State Circuits,* vol. 48, no. 1, pp. 199-213, 2013.

[8] "IEEE approved draft standard for safety levels with respect to human exposure to electric, magnetic and electromagnetic fields, 0 Hz to 300 GHz," *IEEE PC95.1/D3.5, October 2018,* pp. 1-312, 2019.

[9] N. Xing, and G.A. Rincón-Mora, "180-nm 85%-efficient inductively coupled switched resonant half-bridge power receiver," *IEEE Transactions on Circuits and Systems II: Express Briefs,* vol. 66, no. 6, pp. 983-987, 2019.

[10] N. Xing, and G.A. Rincon-Mora, "Generating the highest power with a tiny and distant inductively coupled coil," *2016 IEEE 25th International Symposium on Industrial Electronics*, pp. 477-80, June, 2016

[11] H. Marques, B. Borges, *et al.*, "Contactless battery charger for composite humidity and temperature wireless sensors," *IEEE International Conference on Computer as a Tool*, pp. 4, April, 2011

[12] J.T. Hwang, D.S. Lee, *et al.*, "An all-in-one (Qi, PMA and A4WP) 2.5W fully integrated wireless battery charger IC for wearable applications," *63rd IEEE International Solid-State Circuits Conference, ISSCC 2016, January 31, 2016 - February 4, 2016*, pp. 378-380, 2016

[13] L. Xing, T. Chi-Ying, *et al.*, "Wireless power transfer system using primary equalizer for coupling- and load-range extension in bio-implant applications," *2015 IEEE International Solid-State Circuits Conference (ISSCC), 22-26 Feb. 2015*, pp. 228-9, 2015

[14] C. Lin, K. Wing-Hung, *et al.*, "A 6.78-MHz single-stage wireless power receiver using a 3-mode reconfigurable resonant regulating rectifier," *IEEE Journal of Solid-State Circuits,* vol. 52, no. 5, pp. 1412-23, 05/ 2017.

[15] O. Lazaro, and G.A. Rincon-Mora, "180-nm CMOS wideband capacitor-free inductively coupled power receiver and charger," *IEEE Journal of Solid-State Circuits,* vol. 48, no. 11, pp. 2839-49, Nov. 2013.

[16] O. Lazaro, and G.A. Rincon-Mora, "Inductively coupled 180-nm CMOS charger with adjustable energy-investment capability," *IEEE Transactions on Circuits and Systems II: Express Briefs,* vol. 60, no. 8, pp. 482-6, August 2013.

[17] O. Lazaro, and G.A. Rincon-Mora, "A nonresonant self-synchronizing inductively coupled 0.18-m CMOS power receiver and charger," *IEEE Journal of Emerging and Selected Topics in Power Electronics,* vol. 3, no. 1, pp. 261-271, 2015.

[18] N. Xing, and G. Rincon-Mora, "Highest maximum power point of radially distant inductively coupled power receivers with deep submicron CMOS," *IEEE Transactions on Industrial Informatics,* DOI: 10.1109/TII.2019.2910092.

[19] P. Cong, W.H. Ko, *et al.*, "Wireless batteryless implantable blood pressure monitoring microsystem for small laboratory animals," *IEEE Sensors Journal,* vol. 10, no. 2, pp. 243-254, 2010.

[20] W. Hayward, *Introduction to radio frequency design*: American Radio Relay League, 1994.

[21] M.H. Perrott, T.L. Tewksbury, *et al.*, "A 27 mW CMOS fractional-N synthesizer/modulator IC," *IEEE International Solids-State Circuits Conference*, pp. 366-367, Feb. , 1997

[22] T. Jang, N. Xing, *et al.*, "A 0.026mm^2 5.3mW 32-to-2000MHz digital fractional-N phase locked-loop using a phase-interpolating phase-to-digital converter," *IEEE International Solid-State Circuits Conference*, pp. 254-255, Feb., 2013

[23] N. Xing, and G.A. Rincon-Mora, "Power analysis and maximum output-power scheme for inductively coupled resonant power receivers," *IEEE International Midwest Symposium on Circuits and Systems*, pp. 293-6, August, 2017

[24] Y. Lee, "RFID coil design," *Microchip Design Note,* no. AN678, 1998.

[25] K. Fotopoulou, and B.W. Flynn, "Wireless power transfer in loosely coupled Links: coil misalignment model," *IEEE Transactions on Magnetics,* vol. 47, no. 2, pp. 416-430, 2011.

[26] L. Xing, T. Chi-Ying, *et al.*, "A 13.56 MHz wireless power transfer system with reconfigurable resonant regulating rectifier and wireless power control for implantable medical devices," *IEEE Journal of Solid-State Circuits,* vol. 50, no. 4, pp. 978-89, April 2015.

[27] K. Tomita, R. Shinoda, *et al.*, "1-W 3.3–16.3-V boosting wireless power transfer circuits with vector summing power controller," *IEEE Journal of Solid-State Circuits,* vol. 47, no. 11, pp. 2576-2585, 2012.

[28] M. Kiani, B. Lee, *et al.*, "A Q-Modulation technique for efficient inductive power transmission," *IEEE Journal of Solid-State Circuits,* vol. 50, no. 12, pp. 2839-2848, 2015.

[29] S. Shin, M. Choi, *et al.*, "A 13.56MHz time-interleaved resonant-voltage-mode wireless-power receiver with isolated resonator and quasi-resonant boost converter for implantable systems," *2018 IEEE International Solid - State Circuits Conference - (ISSCC)*, pp. 154-156, 11-15 Feb. 2018, 2018

[30] H.S. Gougheri, and M. Kiani, "Current-based resonant power delivery with multi-cycle switching for extended-range inductive power transmission," *IEEE Transactions on Circuits and Systems I: Regular Papers,* vol. 63, no. 9, pp. 1543-52, 2016.

[31] C. Myungjoon, J. Taekwang, *et al.*, "A resonant current-mode wireless power receiver and battery charger with -32 dBm sensitivity for implantable systems," *IEEE Journal of Solid-State Circuits,* vol. 51, no. 12, pp. 2880-92, Dec. 2016.